Advances in Water Resources 128 (2019) 206–217

Contents lists available at ScienceDirect

Advances in Water Resources

journal homepage: www.elsevier.com/locate/advwatres

A double-continuum transport model for segregated porous media: Derivation and sensitivity analysis-driven calibration

G. Ceriotti[a,*], A. Russian[a], D. Bolster[b], G. Porta[a]

[a] Dipartimento Ingegneria Civile ed Ambientale, Politecnico di Milano, Piazza Leonardo da Vinci, 32, Milano I-20133, Italy
[b] Department of Civil and Environmental Engineering and Earth Sciences, University of Notre Dame, IN, USA

A B S T R A C T

We derive a novel double-continuum transport model based on pore-scale characteristics. Our approach relies on building a simplified unit cell made up of immobile and mobile continua. We employ a numerically resolved pore-scale velocity distribution to characterize the volume of each continuum and to define the velocity profile in the mobile continuum. Using the simplified unit cell, we derive a closed form model, which includes two effective parameters that need to be estimated: a characteristic length scale and a parameter, R_D, given by the ratio of characteristic times that lumps the effect of stagnant regions and escape process. To calibrate and validate our model, we rely on a set of pore-scale numerical simulation performed on a 2D disordered segregated periodic porous medium, taking into account different initial solute distributions. Using a Global Sensitivity Analysis, we explore the impact of the two effective parameters on solute concentration profiles and thereby define a Sensitivity Analysis driven criterion for model calibration. The latter is compared to a classical calibration approach. Our results show that, depending on the initial condition, the mass exchange process between mobile and immobile continua impact on solute profile shape significantly. Our transport model is capable of interpreting both symmetric and highly skewed solute concentration profiles. Effectiveness of the calibration of the two parameters largely depends on the calibration dataset and the selected objective function whose definition can be supported by the implementation of sensitivity analysis. By relying on a sensitivity analysis driven calibration, we are able to provide an accurate and robust interpretation of the concentration profile evolution across different given initial conditions by relying on a unique set of effective parameter values.

1. Introduction

The development of accurate mathematical models to describe solute mass transport in porous media is particularly challenging when the medium is characterized by the presence of cavities, dead-end pores, stagnant zones, and a highly heterogeneous velocity field. The structure and the extent of low-velocity regions directly impact solute transport, potentially leading to long mass retention times. Accurately modeling such trapping effects is crucial, for example, in the context of remediation and risk assessment (e.g. de Barros et al., 2013). A sound understanding of the conditions and pore-scale processes that physically control the rate of exchange between stagnant and fast-flowing regions is needed to better understand solute spreading and mixing and subsequently the evolution of conservative and reactive transport processes (e.g. Alhashmi et al., 2015; Lichtner and Kang, 2007; Kitanidis and Dykaar, 1997; Wirner et al., 2014; Cortis and Berkowitz, 2004; Briggs et al., 2018; Baveye et al., 2018).

Solute transport has been widely studied by performing direct numerical simulations at the pore scale (see e.g. Scheibe et al., 2015; Bijeljic et al., 2013b; Hochstetler et al., 2013; Porta et al., 2013). Such techniques present the remarkable advantage of providing detailed information on solute concentration evolution at each point of the porous domain. However, the applicability of such methods, which are computationally demanding, is limited to small domains, typically much smaller than field scales of common interest (Dentz et al., 2011). Upscaled continuum models are consequently more suited to simulating larger-scale systems.

To upscale the effects of low-velocity regions on emerging transport features, different approaches have been proposed such as Multi-Rate Mass Transfer Model (MRMT, Tecklenburg et al., 2016; Haggerty and Gorelick, 1995; Carrera et al., 1998), various Continuous Time Random Walk approaches (CTRW, Berkowitz and Scher, 2009, 1997; Le Borgne et al., 2008; Dentz and Castro, 2009), time and space-fractional models (fADE, Kelly et al., 2017; Berkowitz et al., 2002), Time Domain Random Walk approaches (TDRW, Banton et al., 1997; Delay et Bodin, 2001; Russian et al., 2016) and other nonlocal formulations (Neuman and Tartakovsky, 2009). In particular, double or multiple continua approaches are appealing due to their ability to explicitly distinguish stagnant zones from fast flowing channels.

In the classical double-continuum approach (Haggerty and Gorelick, 1995; Carrera et al., 1998; Bear and Cheng, 2010), a mobile and immobile continuum exchange mass as a first-order process with an effective mass transfer coefficient. Typically, effective parameters of double or multi-continuum models, need to be estimated via fitting against solute

* Corresponding author.
E-mail address: giulia.ceriotti@polimi.it (G. Ceriotti).

https://doi.org/10.1016/j.advwatres.2019.04.003
Received 22 October 2018; Received in revised form 29 March 2019; Accepted 6 April 2019
Available online 10 April 2019
0309-1708/

concentration data, e.g., measured breakthrough curves or solute concentration profiles.

Alternatively, upscaled dual continua models have been formally derived (see e.g., Souadnia et al., 2002) by means of volume-averaging techniques. While appealing due to their sound theoretical basis, as discussed by Davit et al. (2012), these formally derived double-continua formulations present practical limitations in terms of their applicability to real problems. Often such models can be nearly as difficult to solve as their pore-scale direct simulation counterparts, as they include complex non-local terms, which imply significant numerical implementation challenges (Porta et al., 2016).

As a consequence, a number of studies have proposed more parsimonious effective up-scaled formulations that, however, still exploit key pore scale information. These studies encompass Eulerian (Porta et al., 2015) and Lagrangian formulations (Sund et al., 2017a,b; Dentz et al., 2018). These methods are designed to embed pore-scale characteristics into effective parameters which can be applied at a larger scale. For example, Sund et al. (2017a,b) employ trajectories and travel times distributions measured numerically at pore-scale to infer the effective evolution of mixing and reaction rates in an effective Lagrangian spatial Markov model. The work of Porta et al. (2015) focuses on the use of pore-scale information to characterize a double-continuum transport model, from an Eulerian perspective. Porta et al. (2015) model relies on the cumulative distribution function of velocity measured from a pore-scale simulation of single-phase flow and assumes that the exchange time between high and low velocity regions is dictated by the characteristic diffusion time scale. The model reproduces observed transport behaviors in relatively well connected three-dimensional porous systems, i.e. a beadpack and a sandstone sample. However, as shown by Bénichou and Voituriez (2008), realistic cavities may be characterized by complex geometry such that it can take an extremely long time to exchange mass from slow regions to faster flowing channels. For this reason, the double-continuum approach proposed by Porta et al. (2015) might suffer limitations when the geometry of the porous medium is highly tortuous and presents significant stagnant cavities. Such features may arise in both three-dimensional (e.g. carbonate rocks, see Bijeljic et al., 2013a) and two dimensional porous media which are often employed in simulations and experiments (Acharya et al., 2007; Wirner et al., 2014; de Anna et al., 2014).

Starting from the model developed in Porta et al. (2015), we develop a double-continuum model, which explicitly accounts for a characteristic time for the exchange process between high and low velocity regions which may be larger than the diffusion time scale. This model lumps the effect of exchange process at pore-scale into a single effective parameter, which is defined as the ratio of the time required by the solute to escape/explore the stagnant regions of the porous medium to the characteristic diffusive time scale. Our main objective is to derive a closed form double continuum model and to test it against numerical pore-scale simulations of solute transport performed in a disordered synthetic two-dimensional porous medium, considering different initial conditions.

We explore the flexibility of the model by means of a sensitivity analysis. We assess the effectiveness of the model by means of *i*) a qualitative inspection of concentration profiles predicted considering different initial conditions and *ii*) quantification of the Sobol' indices of appropriately defined target metrics. We also investigate the role of a Global Sensitivity Analysis (GSA) in defining a tailor-made objective function to increase the efficacy of model calibration.

The paper is structured as follows. In Section 2 we present the problem setup that will be used as the test bed for the proposed double continuum model, along with details on the pore-scale model. In Section 3, we derive the proposed closed form double continuum model. In Section 4, the flexibility of the model is explored via a GSA. Calibration and validation of the model are discussed in Section 5 and conclusions are presented in Section 6.

2. Problem setting

2.1. Pore scale domain

In this work, we consider a two-dimensional porous medium made up of repeating periodic unit cells, Ω'. The cell configuration is the same as that of Porta et al. (2016). The geometry of the unit cell is generated by the disordered superposition of circular grains of uniform diameter $w = 8 \times 10^{-5}$ m and then discretized into pixels of 2×10^{-5} m. The resulting pixelated image, characterized by porosity $\phi = 0.5948$, constitutes the reference cell configuration for the pore-scale numerical simulations. While this porosity value is larger than the one typically observed for three-dimensional porous media, two-dimensional porous media with porosities equal or higher than the one considered here are commonly used in previous experimental and numerical studies (see e.g., Wirner et al., 2014; Acharya et al., 2007; de Anna et al., 2014). The domain is periodic in both longitudinal and transversal directions. The fluid flow in the unit cell is driven imposing a unit gradient pressure along the longitudinal direction and zero pressure gradient along the transverse direction. The velocity field is steady and laminar and computed by solving the incompressible Navier-Stokes equations, assuming a fully saturated medium and considering impermeable boundary conditions on the grain-liquid interface (see Porta et al., 2016). The velocity field is resolved on a regular spatial grid with a resolution of 2×10^{-5} m and the numerical approximation is obtained following the methods introduced by Bekri et al. (1995) and Coelho et al. (1997). The grid resolution is one order of magnitude smaller than the average grain size, which is estimated to 214 μm (as given by ImageJ/Fiji imaging processing software Ferreira and Rasband, 2012). The porous medium permeability along the longitudinal direction is equal to 4.87×10^{-5} cm^2. The latter is estimated through the Darcy's law where the total flow discharge and the pressure drop is computed using the numerically resolved pressure and velocity field. The resulting value of permeability is of the same order of magnitude of those associated with clean sand and gravel (see Bear and Cheng, 2010) and thus comparable with real porous systems. The geometry of the unit cell and the associated normalized velocity field (normalized such that the mean velocity modulus is equal to 1) is shown in Fig. 1a. A unit cell has a total dimension of 4.8×10^{-3} m (longitudinal to the main flow direction) times 1.2×10^{-3} m (transverse to the main flow direction). The total length D of the porous domain is equal to 0.192 m, corresponding to a sequence of 40 unit cells. The average velocity along the x-axis (U[ms^{-1}]) is equal to 6.22×10^{-5} ms^{-1}. The velocity field shows large variability, ranging over 10 orders of magnitude.

The probability density function (*pdf*) of velocity is similar to the one observed in real three-dimensional porous media such as sandstones. In Fig. 1b, we compare the *pdf* observed for two real 3D geometries, i.e., Bentheimer Sandstone ($\phi = 0.2147$) and Doddington Sandstone ($\phi = 0.1949$) presented by Alhashmi et al. (2016), against the *pdf* of the local velocities computed for our 2D geometry. This comparison supports that the two-dimensional system considered in our work presents a similar occurrence of low-velocity regions as the one observed in three-dimensional porous media.

We define low-velocity regions as those below 10^{-2} in the normalized velocity field. These regions are segregated from the well-connected higher-velocity channels. We use this value to distinguish between the disconnected Low-Velocity (LV) regions and the continuous High-Velocity (HV) channels. In Fig. 1c we explicitly identify the solid phase and the LV and HV regions. Based on our chosen threshold (10^{-2}), we can split the total porosity ϕ into two parts: $\phi_{HV} = 0.5131$ and $\phi_{LV} = 0.0817$ associated with the HV and LV regions, respectively. The choice of 10^{-2} as velocity threshold between LV and HV regions is here based on a set of preliminary analyses investigating the sensitivity of ϕ_{HV}/ϕ to the velocity threshold. For the chosen geometry we observe that the ratio ϕ_{HV}/ϕ shows minor changes when the velocity threshold varies between 10^{-2} and 10^{-8}.

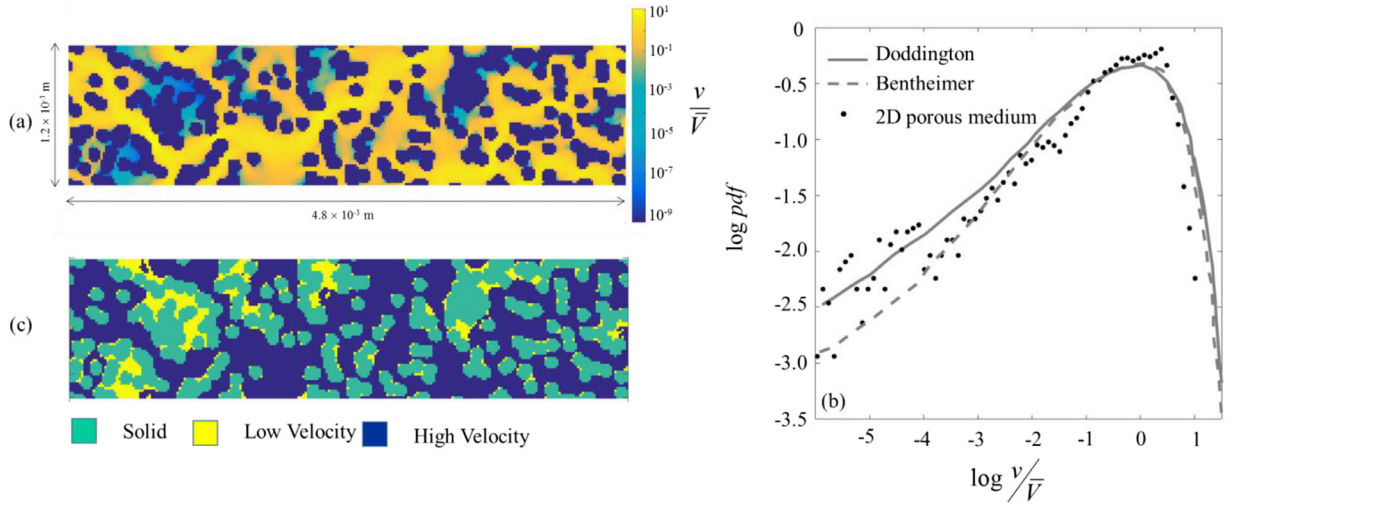

Fig. 1. (a) The geometry of the unit cell with the associated normalized velocity field. (b) Comparison of $v/\bar{V}$ *pdf* computed in the 2D porous medium and in two real 3D samples of sandstones (Doddington and Bentheimer) reported by Alhashmi et al. (2016). (c) The geometry of the low velocity (yellow) and high velocity (blue) regions resulting from imposing 10^{-2} as normalized velocity threshold to discriminate between the low and high velocity regions. (For interpretation of the references to color in this figure legend, the reader is referred to the web version of this article.)

2.2. Initial conditions

The analysis of the impact of the initial solute displacement is a critical feature in assessing the robustness of solute transport models, as recently discussed in Puyguiraud et al. (2019). As a test bed for the double-continuum model that we will present in Section 3, we perform a series of pore-scale simulations of conservative transport with three different initial scenarios, labeled S_U, S_HV and S_LV:

- S_U: in one unit cell the solute is uniformly distributed in both the HV and LV regions. We define the initial concentration as $\bar{E}_0$.
- S_HV: solute is uniformly distributed in only the HV region for the extent of one unit cell. The cross-sectional averaged initial concentration in the HV region ($\bar{E}_{0HV}$) is such that $\bar{E}_0 = \bar{E}_{0HV}\phi_{HV}/\phi$.
- S_LV: solute is uniformly distributed in the LV region for the extent of one unit cell. The cross-sectional averaged initial concentration in the LV region ($\bar{E}_{0LV}$) is such that $\bar{E}_0 = \bar{E}_{0LV}\phi_{LV}/\phi$.

The aforementioned initial conditions are chosen to mimic conditions of particular interest when considering, for example, a contaminated site (e.g. de Barros et al., 2013) or for the interpretation of experimental results, where solute injection in a column is typically flux weighted.

2.3. Pore scale numerical simulations

Pore-scale modeling of the concentration field is performed in a particle tracking framework, with the Time Domain Random Walk (TDRW) approach described in detail in Russian et al. (2016). This approach is particularly suitable for simulations in media that display a broad range of velocity such as the one considered here (Banton et al., 1997; Delay et al., 2002; Bodin, 2015). Classical random walk algorithms are characterized by constant time discretization: random walkers move over variable distances at constant time increments. Alternatively, in the TDRW the domain is spatially discretized and random walkers move over fixed distances in variable time steps. Its benefit is that particles do not spend a large number of random walk steps in low velocity regions due to a constant time discretization. The TDRW method is formally equivalent to a discretized advection-diffusion equation (Russian et al., 2016). At the same time, its formulation coincides with a continuous time domain random walk (CTRW) with space-dependent transition times and probabilities.

Here we use 2 million particles for each simulation. For each initial condition illustrated in Section 2.2, we explore the temporal evolution of concentration over a total time of 400 s. Profile concentrations are obtained by vertical integration of particle numbers normalized by the corresponding porosity of the vertical slice.

3. Dual continuum model formulation

The development of the double-porosity model proposed here is built starting from the procedure originally developed by Porta et al. (2015) and it is schematically outlined in Fig. 2. We start with the 2D-porous medium introduced in Section 2 (Fig. 1). We define the average Péclet number $Pe_{av} = UL/D_m$ where $D_m[\mathrm{m^2 s^{-1}}]$ is the molecular diffusion coefficient and L [m] a characteristic length scale of the system that is considered unknown *a priori* and should be properly determined.

In the double-continuum model, the porous system is then conceptualized as a simplified unit cell of thickness L with a uniform shear flow (Fig. 2a). The direction of flow is only in the $\hat{x}$[m] direction. The unit cell is split into two parts, labeled mobile and immobile. The mobile zone (light color in Fig. 2a) occupies $-l/2 < \hat{y} < l/2$ (with $\hat{y}$ [m]) and the immobile zone (dark color in Fig. 2a) $-L/2 < \hat{y} < -l/2$ and $l/2 < \hat{y} < L/2$. The value of l [m] is computed such that $l/L = \phi_{HV}/\phi$ and $(L-l)/L = \phi_{LV}/\phi$ to partition the mobile/immobile region in the elementary cell in the same manner as the HV and LV regions in the reference porous medium. The velocity distribution in the mobile zone is the (appropriately rescaled) sample cumulative distribution function (*cdf*) from pore-scale velocities belonging to the HV region of the porous medium. In Fig. 2b, we depict the *cdf* computed for the normalized fluid velocity. The vertical dashed line represents the chosen threshold discriminating between HV and LV regions.

We define a dimensionless coordinate reference system introducing $x = \hat{x}/L$ [-] and $y = \hat{y}/L$ [-] where $\hat{x}$ and $\hat{y}$ are the dimensional coordinates reported in Fig. 2a. Using the dimensionless reference system we assume that solute transport in the unit cell is described by the following dimensionless system of equations

$$\begin{cases} \dfrac{\partial E_M}{\partial t} + u\dfrac{\partial E_M}{\partial x} = \dfrac{1}{Pe}\dfrac{1}{\tau_M}\dfrac{\partial^2 E_M}{\partial x^2} + \dfrac{1}{Pe}\dfrac{\partial^2 E_M}{\partial y^2} & |y| < l/(2L) \\ \dfrac{\partial E_I}{\partial t} = \dfrac{1}{Pe}\dfrac{1}{\tau_{IM}}\dfrac{\partial^2 E_I}{\partial x^2} + \dfrac{R_D}{Pe}\dfrac{\partial^2 E_I}{\partial y^2} & |y| > l/(2L) \end{cases} \quad (1)$$

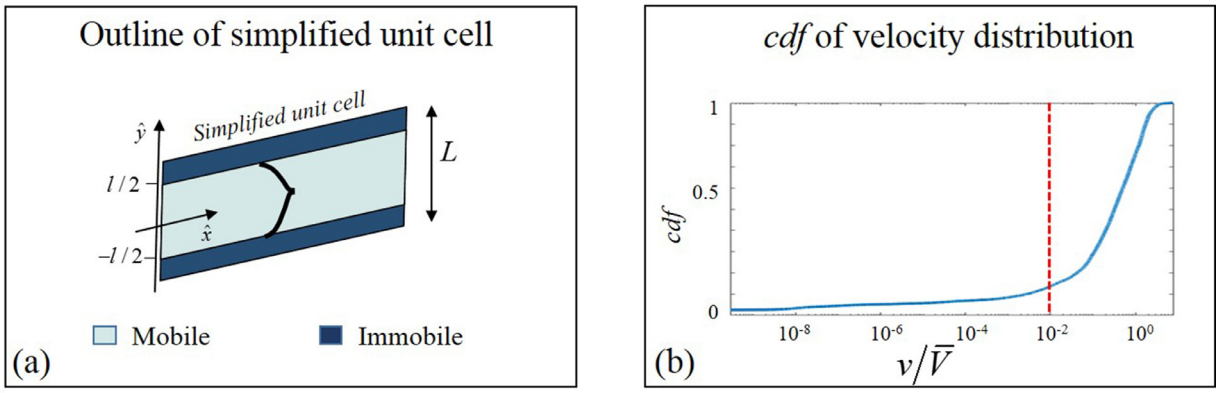

Fig. 2. (a) outline of the simplified unit cell and (b) definition of the Cumulative Density Function (*cdf*) of the local velocities of the fluid phase.

completed by the following boundary conditions

$$\begin{aligned} &E_M = E_I \text{ and } \frac{\partial E_M}{\partial y} = R_D \frac{\partial E_I}{\partial y} && |y|=l/(2L) \quad \text{(a)} \\ &\frac{\partial E_I}{\partial y} = 0 && |y|=1/2 \quad \text{(b)} \end{aligned} \tag{2}$$

where $E_M(x, y, t) = C_{EM}(x, y, t)/c_0$ [-] and $E_I(x, y, t) = C_{EI}(x, y, t)/c_0$ [-] are dimensionless concentrations in the mobile (HV) and immobile (LV) zones of solute E, respectively; $C_{EM}(x, y, t)$[mol L^{-1}] and $C_{EI}(x, y, t)$[mol L^{-1}] are the concentrations in mobile and immobile region, [mol L^{-1}], and c_0, [mol L^{-1}], is a characteristic concentration; u[-] represents the dimensionless velocity along the x-direction computed as the ratio between the dimensional velocity $\hat{u}$ (ms^{-1}) and the mean velocity in the mobile region U_M [ms^{-1}], i.e. $u = \hat{u}/U_M$; t [-] is the dimensionless time defined as $t = \hat{t}/t_a$ where $\hat{t}$ [s] is the time and $t_a = L/U_M$ [s] is the advective time scale; Pe [-] is the Péclet number computed based on the mean mobile velocity as $Pe = U_M L/D_m$.

We introduce in (2) two key novel elements with respect to the formulation of Porta et al. (2015):

- We include the dimensionless parameters τ_M and τ_{IM} that represent the tortuosity factors associated with the HV and LV regions respectively. Including τ_M and τ_{IM} embeds the impact of the phase geometry on the evolution of solute diffusion along the x-direction in the simplified unit cell (Shen and Chen, 2007). The values of τ_M and τ_{IM} are computed directly using the HV and LV geometries, by mean of the TauFactor Matlab code (Cooper et al., 2016; MATLAB® and Statistics Toolbox Release, 2016b). The HV region is characterized by $\tau_M = 2.48$, while τ_{IM} is infinite since the LV region is clearly disconnected (Fig. 1c). The latter is a consequence of considering a two-dimensional porous medium. In more realistic 3D systems, the LV region is connected due to the no-slip boundary condition imposed at the solid-fluid interface and the fact that solid phases connect (unlike in 2D). Here, to mimic a disconnected LV region, we imposed a very high value of tortuosity, $\tau_{IM} = 100$.
- we introduce parameter R_D in (2(a)), defined as

$$R_D = \frac{t_D}{t_e} \tag{3}$$

where t_e [s] is the characteristic time required by the solute to escape/explore the stagnant regions of the porous medium while the t_D [s] is the characteristic time scale of the diffusion process in a free fluid.

In Porta et al. (2015), the mass exchange between HV and LV regions is modeled as a diffusive process at the interface of immobile and mobile zones, which means that the characteristic time of the mass exchange is assumed equal to the characteristic diffusion time $t_D = L^2/D_m$. This choice may not always be appropriate, for example, if the porous structure includes large stagnant cavities connected to fast channels through narrow bottlenecks. Indeed, pore-scale and theoretical investigations (e.g. Wirner et al., 2014; Bénichou and Voituriez, 2008; van Genuchten, 1985; Holcman and Schuss, 2013; Holcman and Schuss, 2004) show that solute mass enclosed in a stagnant (or fast-flowing) region may take an extremely long time to escape (or explore) the zone depending on its shape.

Applying the same averaging procedure implemented by Porta et al. (2015) on the system (2) and (3), the closed section averaged form of the proposed model reads (see the Supplementary Material for more details)

$$\begin{cases} \dfrac{\partial \bar{E}_M}{\partial t} + \dfrac{\partial \bar{E}_M}{\partial x} + \dfrac{\partial}{\partial x}\left[d_{H1}\dfrac{\partial \bar{E}_M}{\partial x} + d_{H2}\Delta \bar{E}_{MI}\right] \\ = \dfrac{1}{Pe}\dfrac{1}{\tau_M}\dfrac{\partial^2 \bar{E}_M}{\partial x^2} + \dfrac{\phi}{Pe\phi_{HV}}\left(e_1\dfrac{\partial \bar{E}_M}{\partial x} + e_2\Delta \bar{E}_{MI}\right) \\ \dfrac{\partial \bar{E}_I}{\partial t} = \dfrac{1}{\tau_{IM}}\dfrac{1}{Pe}\dfrac{\partial^2 \bar{E}_I}{\partial x^2} - \dfrac{\phi}{\phi_{LV}Pe}\left(e_1\dfrac{\partial \bar{E}_M}{\partial x} + e_2\Delta \bar{E}_{MI}\right) \end{cases} \tag{4}$$

where $\bar{E}_M(x, t)$ and $\bar{E}_{IM}(x, t)$ are the averaged (along the y-direction in the cell) concentrations of the solute in the mobile and immobile regions, respectively, while $\Delta \bar{E}_{MI} = \bar{E}_M - \bar{E}_{IM}$. The effective parameters d_{H1}, d_{H2}, e_1 and e_2 appearing in (5) are defined as follows

$$d_{H1} = \frac{L}{l}\int_{-l/(2L)}^{l/(2L)} b_1 \tilde{u}\,dy;\; d_{H2} = \frac{L}{l}\int_{-l/(2L)}^{l/(2L)} b_3 \tilde{u}\,dy \tag{5}$$

$$e_1 = 2R_D\left.\frac{\partial b_2}{\partial y}\right|_{y=l/(2L)} = 2\left.\frac{\partial b_1}{\partial y}\right|_{y=l/(2L)};\; e_2 = 2R_D\left.\frac{\partial b_4}{\partial y}\right|_{y=l/(2L)} = 2\left.\frac{\partial b_3}{\partial y}\right|_{y=l/(2L)} \tag{6}$$

where b_i ($i = 1, 2, 3, 4$) are four closure variables and $\tilde{u}$ indicates the fluctuation of the velocity along the x direction with respect to the mean velocity. The set of closure variables b_i ($i = 1, \ldots, 4$) can be solved numerically given the known $u(y)$ and $b_i(y)$ in the simplified unit cell. Details on the closure problem and its solution are provided in the Supplementary Materials.

Investigating the specific relationship between porous geometry structure and R_D is beyond the scope of the present work and is postponed to future efforts, but understanding its role on large-scale transport is considered next. For the purposes of this work, the quantity R_D is considered as an effective parameter along with the characteristic length scale L whose characterization based on pore-scale geometry feature is still open to debate and different methodologies have been proposed in literature (see e.g. Bear and Cheng, 2010; Mostaghimi et al., 2012; Siena et al., 2014; Meyer and Bijeljic, 2016; Alhashmi et al., 2016; Dullien, 2012). Moreover, we highlight here that the definition of the unit cell depends on the velocity threshold imposed on the porous medium to distinguish between HV and LV regions. In this study, we select a specific threshold value and focus on the investigation of different transport conditions, as a consequence of different solute distributions. The identification of thresholds to discriminate high and low velocity regions

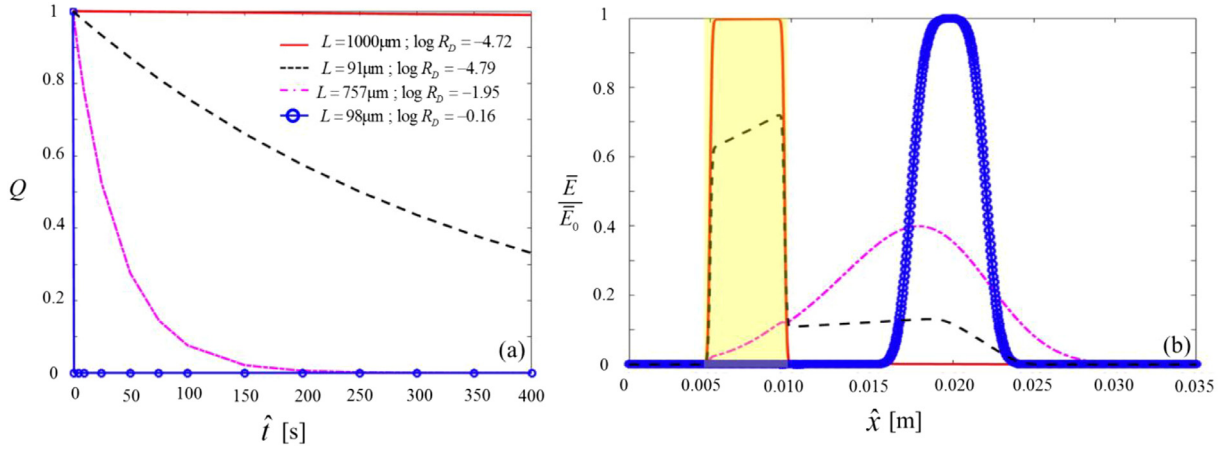

Fig. 3. (a) Temporal evolution of $Q(t)$ for four different combinations of the effective parameters L and R_D computed relying on the S_LV initial scenario; (b) Concentration profiles yielded by model implementation at $\hat{t} = 200$ s for the same four combinations of parameter values and initial scenario reported in panel (a). The shadowed yellow area identifies the location of the solute in the initial condition. (For interpretation of the references to color in this figure, the reader is referred to the web version of this article.)

has been a subject of previous works (see e.g. de Anna et al., 2017; Porta et al., 2015), and may be reconsidered in future works to extend our analysis.

4. Characterization of the mass transfer at the continuum scale

In this Section, we elucidate how the proposed model accounts for the exchange process between fast and slow regions and the impact of the exchange process on solute evolution depending on the initial conditions.

4.1. Quantification of mass transfer time

As a proxy to quantify the exchange process simulated by the model we introduce

$$Q(\hat{t}) = \frac{\left|\langle E_I(\hat{t})\rangle - \langle E_M(\hat{t})\rangle\right|}{E_0} \tag{7}$$

where $\hat{t}$ [s] is time, E_0 is the initial concentration of the conservative solute, $\langle E_I(\hat{t})\rangle$ and $\langle E_M(\hat{t})\rangle$ are the average concentration in the immobile and mobile zones along the x-direction D respectively, i.e.,

$$\langle E_j\rangle = \frac{\int_D \bar{E}_j dx}{V_j} \quad \text{with } j = \text{I, M} \tag{8}$$

with V_M and V_I equal to the pore volume associated with the HV and LV regions of the porous domain. An illustrative example of $Q(\hat{t})$ computed for initial condition S_LV and four combinations of L and R_D is shown in Fig. 3a. We observe that $Q(\hat{t})$ decreases monotonically from 1 to 0 over time. When $Q(\hat{t})$ is equal to 1 all of the solute mass is in the immobile zone, while $Q(\hat{t}) = 0$ indicates an equilibrium between the solute mass flux escaping and entering the immobile zone. How quickly Q reaches zero tells us how quickly the exchange process occurs. The red line ($L = 1000$ μm; $R_D = 1\times10^{-4.72}$) and blue line ($L = 98$ μm; $R_D = 1\times10^{-0.16}$) in Fig. 3a illustrate two extremes cases. For large L and small R_D, $Q(\hat{t})$ suggests an extremely slow escape process such that at 400 s the solute is still almost totally trapped in the immobile zone. This is confirmed in Fig. 3b where we display solute concentration profiles at $\hat{t} = 200$ s for the same combination of L and R_D values of in Fig. 3a. The yellow area identifies the initial step condition. The concentration profile for $L = 1000$ μm and $R_D = 1\times10^{-4.72}$ (red line) coincides closely with the initial condition. By contrast, for small L and R_D close to one, the exchange process is virtually instantaneous since $Q(\hat{t})$ approaches zero in the first time step of the simulation (see blue line in Fig. 3a). The corresponding concentration profile (blue line in Fig. 3b) does not present heavy tailing nor strong asymmetry suggesting that the retentive effect of the stagnant regions is negligible. The black and magenta lines represent intermediate conditions demonstrating that both L and R_D influence the mass exchange process. The four different profiles in Fig. 3b present completely different shapes and spreading patterns, demonstrating that within the context of the proposed model accessibility of the stagnant regions can significantly impact the profile evolution, even when starting from the same initial condition (i.e., S_LV).

4.2. Impact of the initial condition

The value of effective parameters embedded in the formulation 4–6 should depend solely on the porous medium structure and geometry of cavities. This implies that the parameter values should not depend on the initial condition being investigated. By considering different initial conditions as introduced in Section 2, we can compare concentration profiles at $\hat{t} = 200$ s yielded by fixing the values of effective parameters L and R_D (Fig. 4). The combinations of parameters selected for Fig. 4 are those in Fig. 3 for the S_LV scenario. When the exchange process is very fast (magenta and blue lines in Fig. 3a), the impact of the initial condition is virtually not detectable (Fig. 4d). As the exchange process slows down, the initial condition impacts predictions more markedly. The scenarios S_HV and S_U lead to similar profiles in term of spread and skewness; the only notable difference is that the solute with S_U is prone to develop a thicker backward tail (see Fig. 4a–c) as part of the solute is initially entrapped in the immobile zone. The profiles generated starting from the S_HV scenario present a symmetric shape for both very fast and extremely slow exchange process (see Fig. 4b and d). The solute profiles features associated with S_LV are markedly different, as solute has to leave the trapped phase before beginning its downstream journey.

4.3. Global Sensitivity Analysis

The qualitative analysis illustrated above provides a quick understanding of the impact of the exchange process on model predictions, limited to only four combinations of effective parameters selected for presentation purposes. To explore more extensively and rigorously the impact of the variability of the effective parameters on solute transport depending on the initial condition, we investigate different model responses by means of a Global Sensitivity Analysis (Saltelli et al., 2008; Sobol, 1993). Our goal is to explore the sensitivity of the mass transfer process to L and R_D and thereby the resulting impact of mass transfer on the shape of longitudinal concentration profiles under different sce-

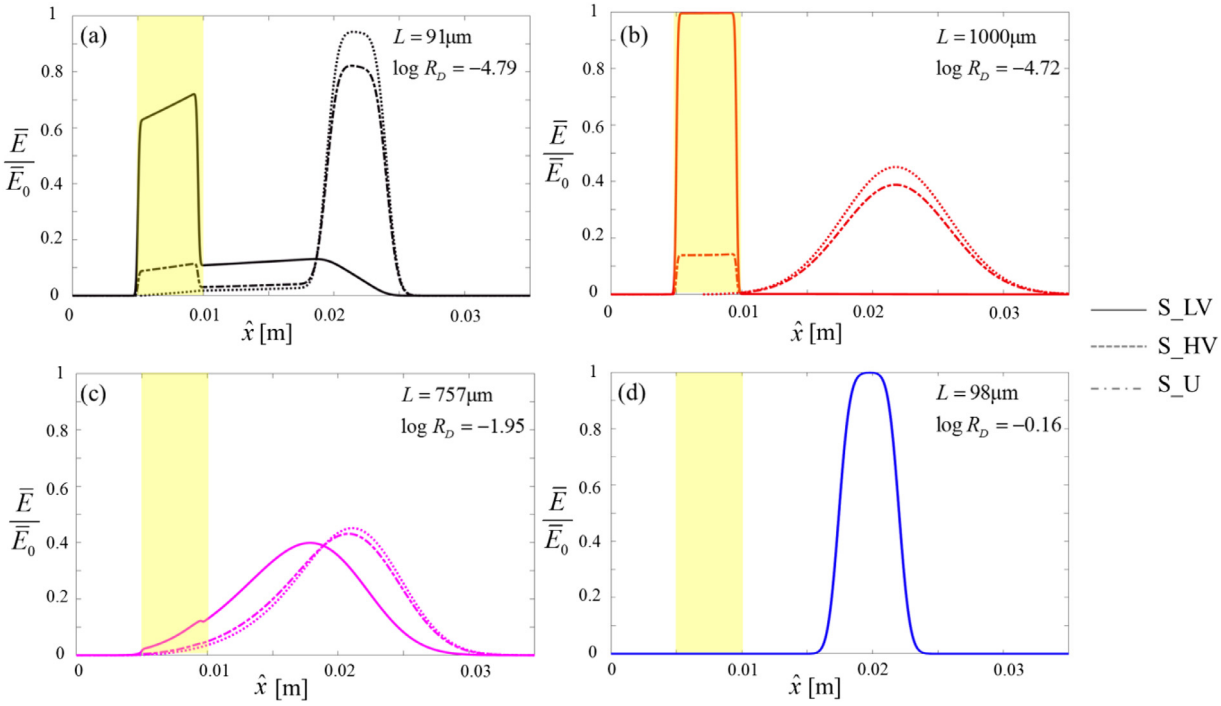

Fig. 4. Concentration profiles given by the solution of Eqs. (4)–(6) at $\hat{t} = 200$ s for S_U, S_HV and S_LV initial conditions with $L = 91$ μm and $R_D = 10^{-4.79}$ (a), $L = 1000$ μm and $R_D = 10^{-4.72}$(b), $L = 757$ μm and $R_D = 10^{-1.95}$ (c) and $L = 98$ μm and $R_D = 10^{-0.16}$(d). The shadowed yellow areas indicate the location where the solute is initially placed.

narios. To this end, we define the following outputs

$$T_{50} = \{\hat{t} | Q(\hat{t}) = 0.5\} \tag{9}$$

$$\sigma^2(\hat{t}) = \int_D \left[\hat{x} - \mu(\hat{t})\right]^2 \bar{E}_n(\hat{x}, \hat{t}) d\hat{x} \tag{10}$$

$$\gamma(\hat{t}) = \frac{\int_D \left[\hat{x} - \mu(\hat{t})\right]^3 \bar{E}_n(\hat{x}, \hat{t}) d\hat{x}}{\sigma^3(\hat{t})} \tag{11}$$

where $\bar{E}_n$ is the section-averaged concentration normalized to total solute mass present in the system and $\mu(\hat{t})$ is the first spatial moment of $\bar{E}_n$. Here, T_{50} [s] is a characteristic time for mass transfer, while σ^2 and γ quantify spreading and skewness of the solute concentration profile. We assume the two effective parameters embedded in the model (i.e. R_D and L) to be two independent uniformly distributed random variables. The parameter L is assumed to vary in Ω_L defined between 80 μm, the diameter of the cylinders used to generate the porous medium (see Section 2), and 1200 μm, i.e. the total length of the periodic unit cell in the transverse direction. The parameter space of R_D (Ω_{RD}) is bounded between 1 and 10^{-5}. The upper bound corresponds to a porous structure that is easily accessible by the solute with the escape/exploration time of the cavities equal to t_D. The lower bound is estimated based on the results of Wirner et al. (2014), who investigate trapping effects of stagnant zones in a quasi two-dimensional porous medium, similar in nature to the one we use here. Using N quasi-Monte Carlo Sobol, 1998) samples ($N = 1000$) of the parameter space $\Omega_L \times \Omega_{RD}$, we run the model for each of the three different initial conditions and compute the first order Sobol' indices associated with the three target variables (9)–(11).

Note that as we consider only two parameters, we can state the following equality by the ANOVA (ANalysis Of VAriance, Sobol, 1993) decomposition of variance

$$SI(k)_L + SI(k)_{RD} + SI(k)_{L,RD} = 1 \quad \text{with} \quad k = T_{50}, \sigma^2, \gamma \tag{12}$$

where $SI(k)_L$ and $SI(k)_{RD}$ are the first order Sobol' indices of variable k associated with parameters L and R_D, respectively, while $SI(k)_{L,RD}$ is the second order Sobol' index quantifying two parameter interaction effects on target quantity k.

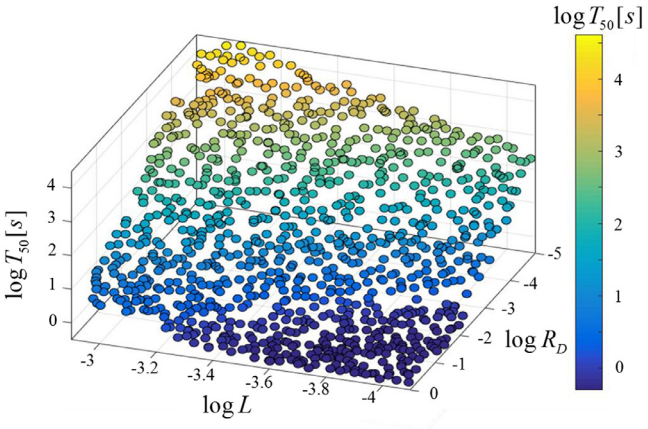

Fig. 5. Evolution of the log T_{50} across the parameter space (i.e., log L and log R_D) for the N sampled combinations of L and R_D, values of L are in meters.

Fig. 5 shows that the characteristic time associated with mass transfer T_{50} is influenced by both parameters so that its variability is explained mostly by the combined variation of the two parameters. This result is quantified by Sobol' indices, which show the largest contribution to the variance of T_{50} is given by the combined effect of the two effective parameters ($SI(T_{50})_{L,RD} = 0.55$, see Table 1). This essentially means that information on both parameters (L and R_D) can help to better constrain this output (and vice versa, i.e. this output, if measurable, could be used to constrain both parameters).

The signature of the results on T_{50} is reflected in a different fashion on profile shapes for different scenarios, as shown in Fig. 6. The Sobol' indices indicate that for scenario S_LV, spreading is mainly influenced by the combined variability of L and R_D because $SI(\sigma^2)_L + SI(\sigma^2)_{RD} < 0.5$

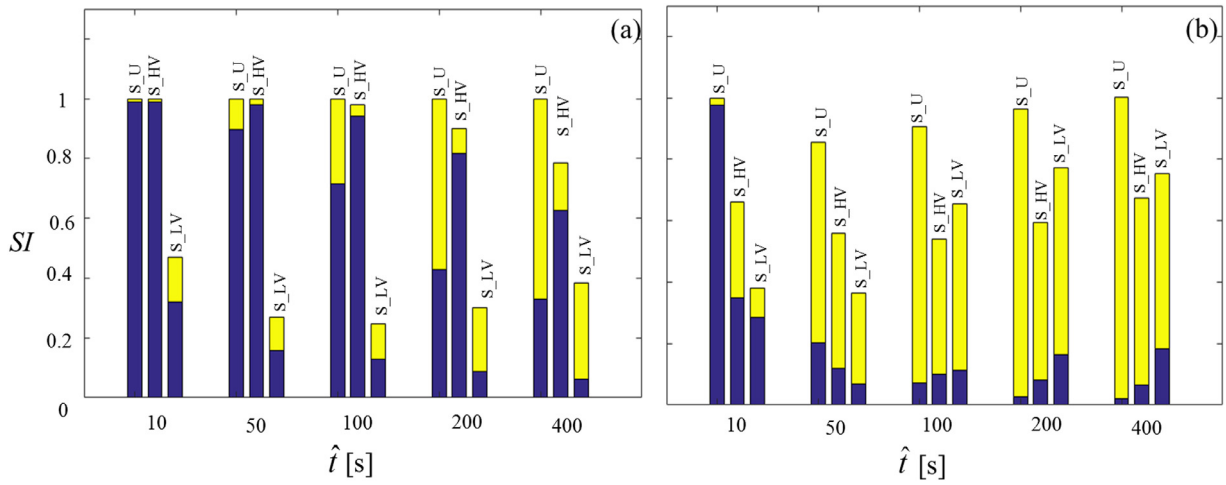

Fig. 6. Sobol' indices computed for (a) the spread of the concentration profile (σ^2) and (b) the skewness of the concentration profiles (γ). Both panels (a) and (b) report the Sobol' indices at five time levels ($\hat{t}$ = 10, 50, 100, 200 and 400 s) for the three different initial scenarios investigated in this work (S_U, S_HV, and S_LV). The blue and yellow portions of the bars quantify $SI(k)_L$ and $SI(k)_{RD}$, respectively, with $k = \sigma^2$, γ. (For interpretation of the references to color in this figure legend, the reader is referred to the web version of this article.)

Table 1
First and second order Sobol' indices computed for the target variable T_{50}.

Index	Sobol' indices value
$SI(T_{50})_L$	0.12
$SI(T_{50})_{RD}$	0.33
$SI(T_{50})_{L,RD}$	0.55

for all the considered times. This is explained by the fact that for S_LV solute displacement is limited by mass transfer to high velocity regions from low velocity regions, where the solute is initially residing. A similar result is obtained for the skewness γ limited to early times. At larger times, γ appears to be chiefly influenced by R_D for S_LV, while the influence of L becomes relatively small after $\hat{t}$ = 50 s. In the S_HV scenario, parameter L almost entirely controls the variance of σ^2 and the chosen length scale has a prominent impact on the solute spread in the mobile region. In this scenario, the solute accesses low velocity regions by mass transfer while being transported downstream. Parameter L has an effect on the *Pe* number and thereby on the spreading of the profile due to dispersion in the mobile region (i.e., dispersive parameters in Eq. (5) increase with L). The effect of R_D and the coupled effect between the two parameters emerge more clearly when profile skewness γ is considered. In particular, γ is chiefly influenced by the joint variation of the two parameters ($SI(\gamma)_L + SI(\gamma)_{RD} < 0.6$) for $\hat{t} > 50$ s. These results show that solute mass transfer has a negligible influence on spreading for S_HV, but is persistently reflected in the profile skewness at long times.

In scenario S_U mass distribution between high and low velocity regions is at equilibrium in the initial condition, i.e. the effect of mass transfer can be expected to be minor compared with the other two cases. Consistent with this observation, spreading σ^2 is initially controlled exclusively by L, while with time the situation is gradually reversed, i.e. R_D becomes the most important parameter. At all times $SI(\sigma^2)_L + SI(\sigma^2)_{RD} \approx 1$ and $SI(\gamma)_L + SI(\gamma)_{RD} > 0.8$, showing that the two parameters act independently to influence the profile shape in scenario S_U.

5. Model calibration and validation

In Section 4, we showed that the proposed model is flexible and able to reproduce symmetric, highly skewed profiles or entrapped solute for an extremely long time by opportunely setting two effective parameters L and R_D. In this Section, we discuss calibration and validation of the model against pore-scale simulations performed in the two-dimensional porous medium from Section 2.

Table 2
Maximum likelihood estimated values of R_D and L with the corresponding confidence interval obtained by implementing *OBF* as an optimization criterion for the calibration procedure applied to pore-scale average concentration data at $\hat{t}$ = 100 s and S_HV.

Parameter	Estimated value	Confidence interval
L [μm]	743	[673, 819]
R_D	$10^{-1.011}$	$[10^{-1.3257}, 10^{-0.6963}]$

5.1. Model calibration

Calibration of the continuum model is performed through the minimization of two different objective functions: *OBF* and a Sensitivity Oriented Objective Function (*SOOF*). We define *OBF* as

$$OBF = \sum_{i=1}^{DC} \left[E(\hat{x}_i) - E_i^*\right]^2 \tag{13}$$

where $\bar{E}(\hat{x}_i)$ is the concentration from the continuum model at $\hat{x}_i$ while $E_i^*(\hat{x}_i)$ is the section-average concentration from the pore-scale simulations. *DC* is the number of data used in the calibration. To compute E^*, we use the same discretization as for the velocity field grid. Objective functions like that in (13) are commonly used to estimate effective model parameters for solute transport (e.g., Porta et al., 2016; Hochstetler and Kitanidis, 2013; Sanchez-Vila et al., 2010) since concentration profiles are a typical experimental observable (e.g. Gramling et al., 2002; Berkowitz et al., 2000; Ye et al., 2015; Molins et al., 2014; Molins et al., 2012). We employ *OBF* in the maximum likelihood framework (Carrera and Neuman, 1986) to estimate L and R_D considering the concentration profile at $\hat{t}$ = 100 s for only the S_HV initial condition. This choice is consistent with the common practice of characterizing transport parameters in scenarios where the solute is injected in the porous domain in a flux-weighted fashion. The estimated values of L and R_D and corresponding variability inferred from the estimated standard deviations (as given by the approximated parameter covariance matrix, see Carrera and Neuman, 1986) are reported in Table 2.

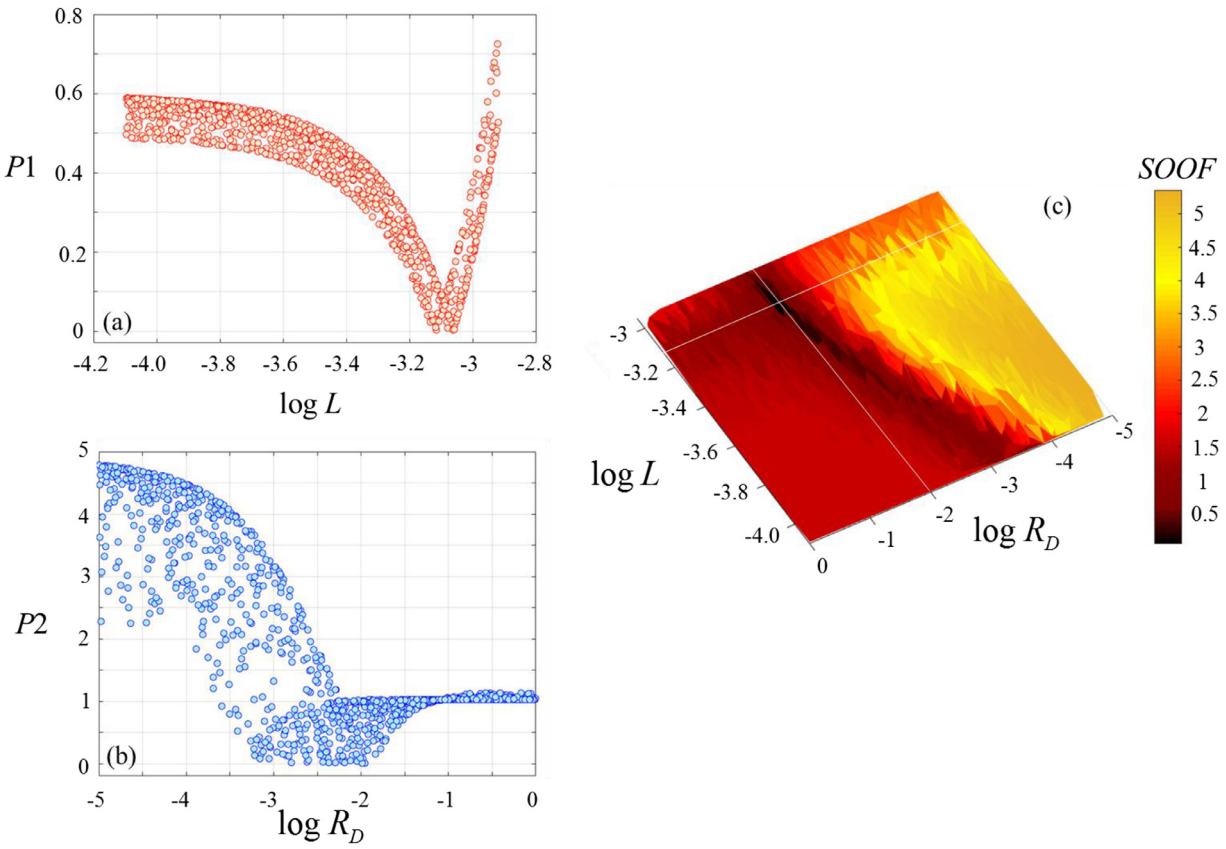

Fig. 7. (a) Evolution of $P1$ as a function of log L and (b) evolution of $P2$ as a function of log R_D computed for the N combinations of parameter explored in the sensitivity analysis, values of L are in meters. The shadowed (red and blue) areas represent the interval of parameters where the $P1$ and $P2$ quantities approach the minimum value. Panel (c) presents the evolution of *SOOF* throughout the parameter space explored in the sensitivity analysis. The solid white lines indicate the likely location of the minimum of the *SOOF*. (For interpretation of the references to color in this figure legend, the reader is referred to the web version of this article.)

Successively, as an alternative to *OBF*, we define a sensitivity oriented objective function *SOOF* as

$$P1 = \left| 1 - \frac{\sigma^2{}_M}{\sigma^2{}_{PS}} \right| \tag{14}$$

$$P2 = \left| 1 - \frac{\gamma_F}{\gamma_{PS}} \right| \tag{15}$$

$$SOOF = P1 + P2 \tag{16}$$

where γ_F and γ_{PS} represent the skewness computed from the double-continuum model and pore-scale model implementation, respectively, at $\hat{t} = 400$ s considering the S_U initial condition. Quantities $\sigma^2{}_M$ and $\sigma^2{}_{PS}$ indicate the spread yielded by the continuum model and pore-scale model, respectively, at $\hat{t} = 50$ s considering the S_HV initial scenario. The objective function *SOOF* is specifically chosen based on the result of our sensitivity analysis (Razavi and Gupta, 2015; Pianosi et al., 2016). Based on the Sobol' sensitivity indices in Fig. 6, we highlight that σ^2 in the S_HV scenario shows a substantial sensitivity to L, especially for early time ($\hat{t} = 10$ s and 50 s) while γ presents a marked sensitivity to R_D at large time. This is corroborated by further inspection of the evolution of $P1$ and $P2$ through the parameter spaces Ω_L (Fig. 7a) and Ω_{RD} (Fig. 7b), respectively.

In Fig. 7a and b we depict the evolution of $P1$ and $P2$ respectively for all combinations of parameters explored in the sensitivity analysis. The trend of $P1$ clearly suggests the presence of a minimum on the interval IL, i.e., $IL = [763\,\mu m, 863\,\mu m]$. Note that the confidence interval and the best estimate reported in Table 2 are in agreement with this interval IL. $P1$ shows steep gradients outside IL which is a desired feature of the objective function when dealing with the calibration process. In Fig. 7b the $P2$ is displayed as a function of R_D. $P2$ approaches its minimum in the interval $IR_D = [10^{-2.37}, 10^{-1.955}]$. Note that the best estimate and the confidence interval of R_D in Table 2 do not correspond to the indications given by the $P2$ criterion. This is further discussed in Section 5.2. Similar to criterion $P1$, $P2$ shows a unique minimum located in a delimited area of the parameter space.

Criterion *SOOF* combining the quantities $P1$ and $P2$ results in an objective function sensitive to both parameters included in the continuum model. By observing the value of *SOOF* over the parameter space investigated in the sensitivity analysis (Fig. 7c), we note that it has a global minimum corresponding to the intersection of the two white solid lines. *SOOF* is minimized using the *fmincon* Matlab function leading to $L = 673.4\,\mu m$ and $R_D = 10^{-1.9972}$ which lie in IL and IR_D, respectively.

5.2. Model validation and discussion

In Fig. 8, we present the comparison between the solute concentration profiles yielded by the model and the section averaged pore-scale data E^* at different times ($\hat{t} = 50$, 100, 200 and 400 s). The dashed lines represent the continuum model results using $L = 743\,\mu m$ and $R_D = 10^{-1.011}$ based on *OBF* as discussed in Section 5.1. The solid lines indicate the continuum model profiles obtained for $L = 673.4\,\mu m$ and $R_D = 10^{-1.9972}$ based on *SOOF*. Fig. 8a–c corresponds to the three different initial conditions, i.e. S_HV (Fig. 8a), S_U (Fig. 8b) and S_LV (Fig. 8c). For simplicity, we refer to M1 and M2 as predictions by the continuum model calibrated according to *OBF* and *SOOF*, respectively.

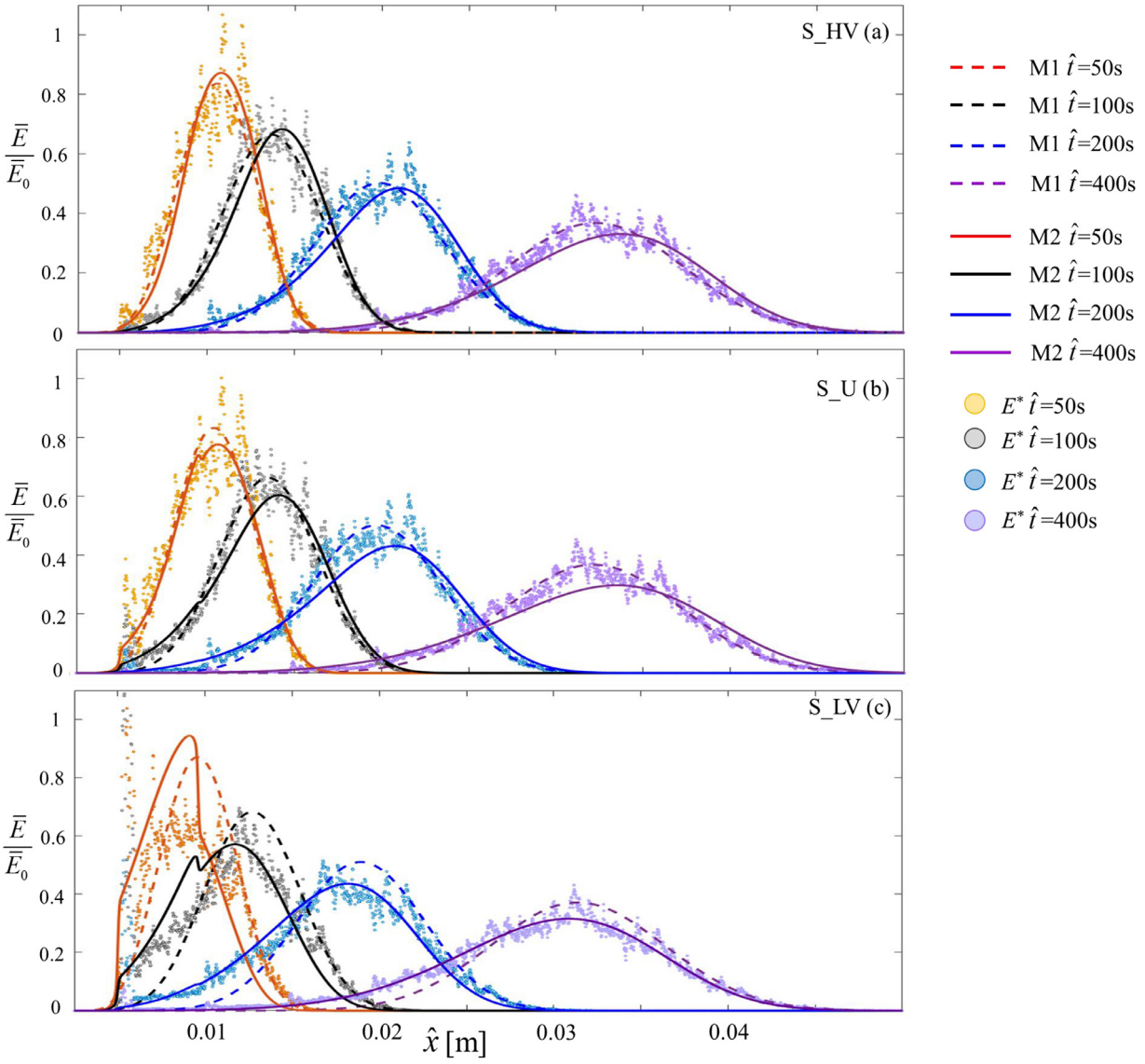

Fig. 8. Comparison of concentration profiles yielded by M1 (dashed lines), M2 (solid lines) and pore-scale model (circles) at $\hat{t}$ = 50, 100, 200 and 400 s associated with S_HV (a), S_U (b) and S_LV (c) scenarios.

In Fig. 8a, both M1 and M2 demonstrate good performance for scenario S_HV. The predictions of M1 and M2 are very close, leading to similar values of concentration peak, spread and shape for all the times investigated. A closer inspection reveals that at $\hat{t}$ = 100 s M1 better matches the pore-scale profile, consistent with the definition of *OBF*. At larger times ($\hat{t}$ = 200 s and $\hat{t}$ = 400 s) a qualitative analysis suggests that M1 tends to match closely the frontward tail while M2 shows more accuracy in reproducing the backward tail. We avoid quantitative comparison given the intense fluctuations from the pore-scale data, which may yield misleading results.

The formulation of the continuum model presented in Sections 3 and 4 embeds the effect of pore-scale processes in the two effective parameters L and $R_{D,}$ which should depend only on pore structure and geometry. If so, in principle, the estimated parameters relying on *OBF* should be exportable to the prediction of solute concentrations obtained in S_LV and S_U, even though these scenarios were not part of the calibration process. For S_U (Fig. 8b), M1 provides a good interpretation of the forward tail and the concentration peak but tends to underestimate the backward tail. This is clear especially at $\hat{t}$ = 100 s and $\hat{t}$ = 200 s. Concerning S_LV, M1 poorly interprets pore-scale data: the backward tail is markedly underestimated while the concentration peak is overestimated for all considered times shown in Fig. 8c. Model M1 only presents a good match with data associated with fast flowing solute, i.e. a small portion of the frontward concentration tail. This is because M1 is calibrated to describe the mobile solute as shown in Fig. 8a.

Based on the results in Fig. 8, we can assert that the classical *OBF* allows calibration of a model with enough accuracy to predict concentration profiles at all times when the same initial condition is explored. However, we show that *OBF* may not be appropriate to estimate parameter values intended to be implemented for diverse initial conditions.

The combination of effective parameters (i.e. $L = 673.4\,\mu m$ and $R_D = 10^{-1.9972}$) associated with M2 leads to improved predictions of the profiles for S_U and S_HV when compared to M1. In Fig. 8b, M2 and M1 are virtually indistinguishable at $\hat{t}$ = 50 s, but M2 better captures the behavior of the backward tail at longer times. This result is obtained by explicitly incorporating information on the skewness of the profile, which carries the necessary information to constrain R_D (Fig. 6). As the length scale in M1 ($L = 743\,\mu m$) is close to that of M2 ($L = 673.4\,\mu m$), we expect that the improved interpretation of the backward tails in Fig. 8b is mainly attributable to the different order of magnitude in the estimate

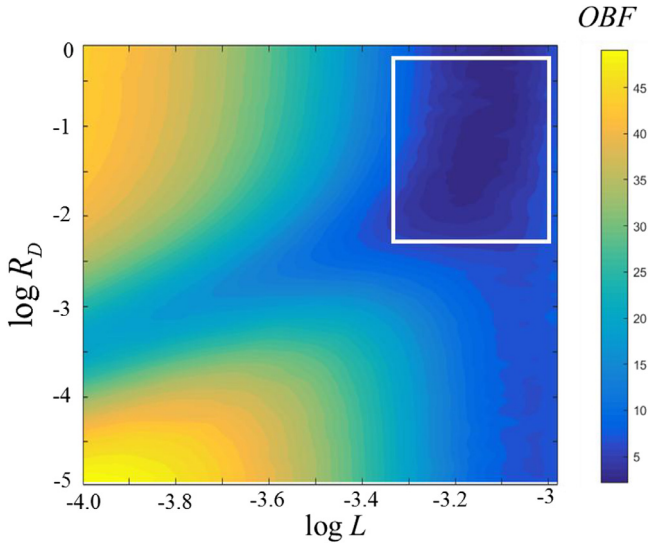

Fig. 9. Evolution of the *OBF* across the parameter space. The white rectangle indicates the range of the parameter space where the *OBF* approaches the smallest values in the parameter space explored.

of R_D. Concerning the S_LV scenario, M2 shows excellent performance in reproducing the larger times ($\hat{t}$ = 200, 400 s) and matching the peak of solute concentration at $\hat{t}$=100 s even as it fails in capturing the exact profile shape at early times, i.e. $\hat{t}$ = 100 s and $\hat{t}$ = 50 s (Fig. 8c). The mismatch at early times can be attributed to a limitation of the continuum model, which condenses the escape process from cavities with a single characteristic time scale t_e. This simplifies implementation, but only captures the average behavior of the cavities and not the complete distribution of transit times that may be present (see e.g., Wirner et al., 2014). This limitation is highlighted when considering scenario S_LV where the escape process is crucial for determining concentration evolution.

As discussed in Section 5.1, *SOOF* is tailor-made for this specific model and problem setting based on the sensitivity analysis in Section 4. By investigating the sensitivity, we can explain discrepancies and the reliability of parameter estimates obtained by using *OBF* compared to *SOOF*.

We conclude our analysis by a close inspection of the shortcomings in the implementation of *OBF*. Fig. 9 shows that *OBF* has its minimum in the region, highlighted by the white rectangle. Criterion *OBF* sharply varies with L close to the minimum but has negligible gradients along R_D. This observation suggests that *OBF* is a strong criterion for estimating L. Indeed, the estimated values of L from *OBF* and *SOOF* are consistent and reinforce one another. On the other hand, the identification of an optimal value for R_D is problematic through *OBF*. Thereby, backward tails are not matched by M1. This result is in apparent contrast with the observation that the skewness (γ) of the profile obtained for S_HV is largely influenced by R_D at $\hat{t}$ = 100 s (as indicated by the Sobol' indices $SI(\gamma)_{RD}$ = 0.43, see Fig. 6), which would suggest that these data are appropriate to properly estimate R_D. By looking at Fig. 9, we can note that the sensitivity of *OBF* to R_D is not uniform across the parameter space for values of L larger than 500 μm (i.e., log L > -3.3). This result agrees with previous observations that global sensitivity measures are effective in identifying general trends but may overlook local sensitivities, which are eventually relevant in a parameter estimation context (see also, Ceriotti et al., 2018).

6. Conclusions

The present work is devoted to the formulation, calibration, and validation of a double-continuum model for solute transport in porous media, which aims to embed characteristics of the pore-scale geometry and velocity field.

As opposed to available non-Fickian transport models (Neuman and Tartakovsky, 2009) or those rigorously derived through Volume Averaging (Davit et al., 2012), our model does not include any nonlocal term, which makes the model implementation straightforward. In spite of this simplification, the method can reproduce features commonly observed in porous media with essentially disconnected micro- and macro-pores, i.e. single peak to a double peak concentration profile (see de Vries et al., 2017). The switch between different emerging behaviors is governed in our model by two effective parameters, which are explicitly linked to the geometry and the velocity field of the porous medium.

Supported by the efficient sensitivity oriented calibration, our proposed model is able to capture many crucial features of the concentration profile evolution over time for all considered scenarios (see Fig. 8). Thus, despite the simplicity of model structure and the absence of spatial and temporal non local terms that arise in rigorous upscaling approaches, the model shows promising performances, yielding good fits and predictive capabilities to the diverse solute transport scenarios considered here. We are able to identify a unique combination of effective parameters that characterize well, on average, the exchange process based solely on the features of the porous medium and the velocity field. However, its identification is not trivial and depends on the type of calibration data available and the structure of the objective function to be optimized. The use of classical mismatch between data and observations (*OBF*) for model calibration provides parameter estimates that perform well in describing solute transport for the S_HV scenario but these estimates were not exportable to other initial scenarios. In our case study, using a criterion driven by sensitivity analysis results (*SOOF*) for parameter estimation instead of *OBF* leads to an improved characterization of the model effective parameters, especially R_D. This result aligns with the idea that formulating an efficient objective function is a crucial aim along with the model development/implementation depending on the data available and the reference scenario investigated. This clearly suggests that the sensitivity analysis of an effective model can be an efficient tool to design *ad hoc* metrics for model calibration and circumvent the use of weakly sensitive objective functions for parameter estimation.

Moreover, investigating the role played by the different parameters by means of sensitivity analysis allows a better understanding of the solute transport phenomena itself. Our results demonstrate that the impact of the exchange process on the solute profile is significant and can lead to notably different shapes and spreading patterns even when starting from the same initial condition (Fig. 4). Modeling the access/escape process of stagnant zones is crucial for capturing the complex patterns associated with complex real porous media structures, e.g. such as those observed in carbonates.

Our analysis on three different initial conditions clearly suggests that the mass exchange process does not always affect the solute profile evolution: it is possible to observe a perfectly symmetric profile even in porous media characterized by extremely inaccessible cavities and dead end pores depending on the initial condition selected (see Fig. 4b, S_HV, dashed line). This is clearly shown by the Sobol' indices results (Table 1 and Fig. 6) which indicate that the exchange mass process and model parameters have a different impact depending on the initial scenario considered. We can conclude that tracer tests performed for a single initial condition may lead to incomplete knowledge of the porous medium structure and understanding of the impact of mass exchange processes.

Acknowledgments

G. Ceriotti and G.M. Porta would like to thank the EU and MIUR for funding, in the frame of the collaborative international Consortium (WE-NEED) financed under the ERA-NET WaterWorks2014 Co- funded Call. This ERA-NET is an integral part of the 2015 Joint Activities developed by the Water Challenges for a Changing World Joint Programme Initiative (Water JPI).

D. Bolster greatly acknowledges financial support from the U.S. National Science Foundation via grants EAR 1351625 and CBET 1705770.

Supplementary material

Supplementary material associated with this article can be found, in the online version, at doi:10.1016/j.advwatres.2019.04.003.

References

Acharya, R.C., Valocchi, A.J., Werth, C.J., Willingham, T.W., 2007. Pore-scale simulation of dispersion and reaction along a transverse mixing zone in two-dimensional porous media. Water Resour. Res. 43, W10435.

Alhashmi, Z., Blunt, M., Bijeljic, B., 2015. Predictions of dynamic changes in reaction rates as a consequence of incomplete mixing using pore scale reactive transport modeling on images of porous media. J. Contam. Hydrol. 179, 171–181.

Alhashmi, Z., Blunt, M., Bijeljic, B., 2016. The impact of pore structure heterogeneity, transport, and reaction conditions on fluid–fluid reaction rate studied on images of pore space. Transp. Porous Media 115 (2), 215–237.

Banton, O., Delay, F., Porel, G., 1997. A new time domain random walk method for solute transport in 1-D heterogeneous media. Ground Water 35, 1008–1013.

Baveye, P.C., Otten, W., Kravchenko, A., Balseiro-Romero, M., Beckers, E., Chalhoub, M., Darnault, C., Eickhorst, T., Garnier, P., Hapca, S., et al., 2018. Emergent properties of microbial activity in heterogeneous soil microenvironments: different research approaches are slowly converging, yet major challenges remain. Front. Microbiol. 9, 1929.

Bear, J., Cheng, A.H., 2010. Modeling Groundwater Flow and Contaminant Transport. Springer Science & Business Media.

Bekri, S., Thovert, J., Adler, P., 1995. Dissolution of porous media. Chem. Eng. Sci. 50 (17), 2765–2791.

Bénichou, O., Voituriez, R., 2008. Narrow-escape time problem: time needed for a particle to exit a confining domain through a small window. Phys. Rev. Lett. 100 (16), 168105.

Berkowitz, B., Scher, H., 1997. Anomalous transport in random fracture networks. Phys. Rev. Lett. 79 (20), 4038–4041.

Berkowitz, B., Scher, H., 2009. Exploring the nature of non-Fickian transport in laboratory experiments. Adv. Water Resour. 32 (5), 649–654.

Berkowitz, B., Scher, H., Silliman, S.E., 2000. Anomalous transport in laboratory-scale, heterogeneous porous media. Water Resour. Res. 36 (1), 149–158.

Berkowitz, B., Klafter, J., Metzler, R., Scher, H., 2002. Physical pictures of transport in heterogeneous media: advection-dispersion,random-walk, and fractional derivative formulations. Water Resour. Res. 38 (10), 1191.

Bijeljic, B., Mostaghimi, P., Blunt, M.J., 2013a. Insights into non-Fickian solute transport in carbonates. Water Resour. Res. 49 (5), 2714–2728.

Bijeljic, B., Raeini, A., Mostaghimi, P., Blunt, M.J., 2013b. Predictions of non-fickian solute transport in different classes of porous media using direct simulation on pore-scale images. Phys. Rev. E 87 (1), 013011.

Bodin, J., 2015. From analytical solutions of solute transport equations to multidimensional time-domain random walk (TDRW) algorithms. Water Resour. Res. 51 (3), 1860–1871.

Briggs, M.A., Day-Lewis, F.D., Dehkordy, F.M.P., Hampton, T., Zarnetske, J.P., Scruggs, C.R., Singha, K., Harvey, J.W., Lane, J.W., 2018. Direct observations of hydrologic exchange occurring with less-mobile porosity and the development of anoxic microzones in sandy lakebed sediments. Water Resour. Res. 54 (7), 4714–4729.

Carrera, J., Neuman, S.P., 1986. Estimation of aquifer parameters under transient and steady state conditions: 1. maximum likelihood method incorporating prior information. Water Resour. Res. 22 (2), 199–210.

Carrera, J., Sánchez-Vila, X., Benet, I., Medina, A., Galarza, G., Guimerà, J., 1998. On matrix diffusion: formulations, solution methods and qualitative effects. Hydrogeol. J. 6 (1), 178–190.

Ceriotti, G., Guadagnini, L., Porta, G., Guadagnini, A., 2018. Local and global sensitivity analysis of Cr (VI) geogenic leakage under uncertain environmental conditions. Water Resour. Res. 54, 5785–5802.

Coelho, D., Thovert, J., Adler, P.M., 1997. Geometrical and transport properties of random packings of spheres and aspherical particles. Phys. Rev. E 55 (2), 1959.

Cooper, S., Bertei, A., Shearing, P., Kilner, J., Brandon, N., 2016. TauFactor: an open–source application for calculating tortuosity factors from tomographic data. Softwarex 5, 203–210.

Cortis, A., Berkowitz, B., 2004. Anomalous transport in “classical” soil and sand columns. Soil Sci. Soc. Am. J. 68 (5), 1539–1548.

Davit, Y., Wood, B.D., Debenest, G., Quintard, M., 2012. Correspondence between one-and two-equation models for solute transport in two-region heterogeneous porous media. Transp. Porous Media 95 (1), 213–238.

de Anna, P., Jimenez-Martinez, J., Tabuteau, H., Turuban, R., Le Brogne, T., Derrien, M., Méheust, Y., 2014. Mixing and reaction kinetics in porous media: an experimental pore scale quantification. Environ. Sci. Technol. 48 (1), 508–516.

de Anna, P., Quaife, B., Biros, G., Juanes, R., 2017. Prediction of the low-velocity distribution from the pore structure in simple porous media. Phys. Rev. Fluids 2, 124103.

de Barros, F.P.J., Guadagnini, A., Fernàndez-Garcia, D., Riva, M., Sanchez-Vila, X., 2013. Controlling metrics for improved characterization of well–head protection regions. J. Hydrol. 494, 107–115.

de Vries, E.T., Raoof, A., vanGenuchten, M.Th., 2017. Multiscale modelling of dual-porosity porous media; a computational pore-scale study for flow and solute transport. Adv. Water Resour. 105, 82–95.

Delay, F., Porel, G., Sardini, P., 2002. Modelling diffusion in a heterogeneous rock matrix with a time-domain lagrangian method and an inversion procedure. Comptes Rendus Geoscience 334 (13), 967–973.

Delay, F., Bodin, J., 2001. Time domain random walk method to simulate transport by advection-diffusion and matrix diffusion in fracture networks. Geophys. Res. Lett. 28, 4051–4054.

Dentz, M., Castro, A., 2009. Effective transport dynamics in porous media with heterogeneous retardation properties. Geophys. Res. Lett. 36, L03403.

Dentz, M., Icardi, M., Hidalgo, J.J., 2018. Mechanisms of dispersion in a porous medium. J. Fluid Mechanics 841, 851–882.

Dentz, M., Le Borgne, T., Englert, A., Bijeljic, B., 2011. Mixing, spreading and reaction in heterogeneous media: a brief review. J. Contam. Hydrol. 120, 1–17.

Dullien, F.A., 2012. Porous Media: Fluid Transport and Pore Structure. Academic press.

Ferreira, T., Rasband, W., 2012. ImageJ user guide. Imagej/fiji, 1.

Gramling, C.M., Harvey, C.F., Meigs, L.C., 2002. Reactive transport in porous media: a comparison of model prediction with laboratory visualization. Environ. Sci. Technol. 36 (11), 2508–2514.

Haggerty, R., Gorelick, S.M., 1995. Multiple-rate mass transfer for modeling diffusion and surface reactions in media with pore-scale heterogeneity. Water Resour. Res. 31 (10), 2383–2400.

Hochstetler, D.L., Kitanidis, P.K., 2013. The behavior of effective rate constants for bimolecular reactions in an asymptotic transport regime. J. Contam. Hydrol. 144 (1), 88–98.

Hochstetler, D.L., Rolle, M., Chiogna, G., Haberer, C.M., Grathwohl, P., Kitanidis, P.K., 2013. Effects of compound-specific transverse mixing on steady-state reactive plumes: insights from pore-scale simulations and darcy-scale experiments. Adv. Water Resour. 54, 1–10.

Holcman, D., Schuss, Z., 2004. Escape through a small opening: receptor trafficking in a synaptic membrane. J. Stat. Phys. 117 (5–6), 975–1014.

Holcman, D., Schuss, Z., 2013. Control of flux by narrow passages and hidden targets in cellular biology. Rep. Prog. Phys. 76 (7), 074601.

Kelly, J.F., Bolster, D., Meerschaert, M.M., Drummond, J.D., Packman, A.I., 2017. FracFit: a robust parameter estimation tool for fractional calculus models. Water Resour. Res. 53 (3), 2559–2567.

Kitanidis, P.K., Dykaar, B.B., 1997. Stokes flow in a slowly varying two-dimensional periodic pore. Transp. Porous Media 26 (1), 89–98.

Lichtner, P.C., Kang, Q., 2007. Upscaling pore-scale reactive transport equations using a multiscale continuum formulation. Water Resour. Res. 43 (12).

Le Borgne, T., Dentz, M., Carrera, J., 2008. A Lagrangian statistical model for transport in highly heterogeneous velocity fields. Phys. Rev. Lett. 101, 090601.

MATLAB and Statistics Toolbox Release 2016b, The MathWorks, Inc., Natick, Massachusetts, United States https://it.mathworks.com/help/matlab/.

Meyer, D.W., Bijeljic, B., 2016. Pore-scale dispersion: bridging the gap between microscopic pore structure and the emerging macroscopic transport behavior. Phys. Rev. E 94 (1), 013107.

Molins, S., Trebotich, D., Steefel, C.I., Shen, C., 2012. An investigation of the effect of pore scale flow on average geochemical reaction rates using direct numerical simulation. Water Resour. Res. 48 (3), W03527.

Molins, S., Trebotich, D., Yang, L., Ajo-Franklin, J.B., Ligocki, T.J., Shen, C., Steefel, C.I., 2014. Pore-scale controls on calcite dissolution rates from flow-through laboratory and numerical experiments. Environ. Sci. Technol. 48 (13), 7453–7460.

Mostaghimi, P., Bijeljic, B., Blunt, M., 2012. Simulation of flow and dispersion on pore-space images. SPE J. 17 (04), 1131–1141.

Neuman, S.P., Tartakovsky, D., 2009. Perspective on theories of non-Fickian transport in heterogeneous media. Adv. Water Resour. 32, 670–680.

Pianosi, F., Beven, K., Freer, J., Hall, J.W., Rougier, J., Stephenson, D.B., Wagener, T., 2016. Sensitivity analysis of environmental models: a systematic review with practical workflow. Environ. Model. Softw. 79, 214–232.

Porta, G.M., Chaynikov, S., Thovert, J., Riva, M., Guadagnini, A., Adler, P.M., 2013. Numerical investigation of pore and continuum scale formulations of bimolecular reactive transport in porous media. Adv. Water Resour. 62, 243–253.

Porta, G., Bijeljic, B., Blunt, M., Guadagnini, A., 2015. Continuum-scale characterization of solute transport based on pore-scale velocity distributions. Geophys. Res. Lett. 42 (18), 7537–7545.

Porta, G., Ceriotti, G., Thovert, J., 2016. Comparative assessment of continuum-scale models of bimolecular reactive transport in porous media under pre-asymptotic conditions. J. Contam. Hydrol. 185, 1–13.

Puyguiraud, A., Gouze, P., Dentz, M., 2019. Stochastic dynamics of Lagrangian pore-scale velocities in three-dimensional porous media. Water Resour. Res. 55 (2), 1196–1217.

Razavi, S., Gupta, H.V., 2015. What do we mean by sensitivity analysis? the need for comprehensive characterization of “global” sensitivity in earth and environmental systems models. Water Resour. Res. 51 (5), 3070–3092.

Russian, A., Dentz, M., Gouze, P., 2016. Time domain random walks for hydrodynamic transport in heterogeneous media. Water Resour. Res. 52 (5), 3309–3323.

Saltelli, A., Ratto, M., Andres, T., Campolongo, F., Cariboni, J., Gatelli, D., . . . Tarantola, S., 2008. Global Sensitivity Analysis: The Primer. John Wiley & Sons.

Sanchez-Vila, X., Fernàndez-Garcia, D., Guadagnini, A., 2010. Interpretation of column experiments of transport of solutes undergoing an irreversible bimolecular reaction using a continuum approximation. Water Resour. Res. 46 (12).

Scheibe, T.D., Perkins, W.A., Richmond, M.C., McKinley, M.I., Romero-Gomez, P.D., Oostrom, M., Zachara, J.M., 2015. Pore-scale and multiscale numerical simulation of flow and transport in a laboratory-scale column. Water Resour. Res. 51 (2), 1023–1035.

Shen, L., Chen, Z., 2007. Critical review of the impact of tortuosity on diffusion. Chem. Eng. Sci. 62 (14), 3748–3755.

Siena, M., Riva, M., Hyman, J., Winter, C.L., Guadagnini, A., 2014. Relationship between pore size and velocity probability distributions in stochastically generated porous media. Phys. Rev. E 89 (1), 013018.
Sobol, I.M., 1993. Sensitivity estimates for nonlinear mathematical models. Math. Model. Comput. Exp. 1 (4), 407–414.
Sobol', I.M., 1998. On quasi-monte carlo integrations. Math. Comput. Simul. 47 (2), 103–112.
Souadnia, A., Didierjean, S., Moyne, C., 2002. Transient dispersion in porous media: a comparison between exact and approximate solutions in a case study. Transp. Porous Media 47 (3), 245–277.
Sund, N.L., Porta, G.M., Bolster, D., 2017a. Upscaling of dilution and mixing using a trajectory based spatial Markov random walk model in a periodic flow domain. Adv. Water Resour. 103, 76–85.
Sund, N., Porta, G., Bolster, D., Parashar, R., 2017b. A Lagrangian transport eulerian reaction spatial (LATERS) Markov model for prediction of effective bimolecular reactive transport. Water Resour. Res. 53 (11), 9040–9058.
Tecklenburg, J., Neuweiler, I., Carrera, J., Dentz, M., 2016. Multi-rate mass transfer modeling of two-phase flow in highly heterogeneous fractured and porous media. Adv. Water Resour. 91, 63–77.
van Genuchten, M.T., 1985. General Approach for Modeling Solute Transport in Structured Soils.
Wirner, F., Scholz, C., Bechinger, C., 2014. Geometrical interpretation of long-time tails of first-passage time distributions in porous media with stagnant parts. Phys. Rev. E 90 (1), 013025.
Ye, Y., Chiogna, G., Cirpka, O., Grathwohl, P., Rolle, M., 2015. Experimental investigation of compound-specific dilution of solute plumes in saturated porous media: 2-D vs. 3-D flow-through systems. J. Contam. Hydrol. 172, 33–47.